

Research Article

Zn-Doped SnO₂ Compact Layer for Enhancing Performance of Perovskite Solar Cells

Chenjun Yang,¹ Mengwei Chen ,² Jiaqi Wang,² and Haifei Lu²

¹School of Information Engineering, Wuhan University of Technology, Wuhan 430070, China

²School of Science, Wuhan University of Technology, Wuhan 430070, China

Correspondence should be addressed to Mengwei Chen; mengwei.chen@whut.edu.cn

Received 31 March 2021; Accepted 12 June 2021; Published 22 June 2021

Academic Editor: Pierluigi Guerriero

Copyright © 2021 Chenjun Yang et al. This is an open access article distributed under the Creative Commons Attribution License, which permits unrestricted use, distribution, and reproduction in any medium, provided the original work is properly cited.

Perovskite solar cells (PSCs) have been developing rapidly since they were discovered, and their excellent photoelectric properties have attracted wide attention from researchers. The compact layer is an important part of PSCs, which can transport electrons and block holes. SnO₂ is an excellent and commonly used electron transport layer (ETL) material, and doping modification is an effective way to improve performance. Here, Zn with a similar radius to Sn has been introduced to the doping of the SnO₂ compact layer to achieve the purposes of conductivity enhancement of the compact layer and followed photoelectric performance improvement of the device. Zn-SnO₂ compact layers with different doping concentrations were prepared and applied to mesoporous architecture PSCs. When the doping content was 5%, the power conversion efficiency (PCE) of the device based on the Zn-SnO₂ compact layer has increased from 9.08% to 10.21%, with an increase of 12.44%. The doping of SnO₂ promotes its application in low-cost PSCs.

1. Introduction

Organic-inorganic lead hybrid perovskite materials have become the research focus of researchers all over the world due to their advantages of low cost, solution-based preparation method, strong light absorption capacity, adjustable band gap, and long carrier diffusion length. It is also the ideal light-absorbing material for solar cells [1–4]. The first perovskite solar cells (PSCs) came out in 2009, and in a few years, the power conversion efficiency (PCE) of solar cells based on perovskite light-absorbing materials has increased from 3.8% to the current 25.5% [5–16].

PSCs are usually composed of conductive substrate, electron transport layer (ETL), perovskite photosensitive layer, hole transport layer (HTL), and counterelectrode. Perovskite materials have the bipolar properties of electron and hole transport [17–19]. In the development of PSCs, in order to reduce the device cost and simplify the preparation process, devices without HTL and electron free transport layer structure have appeared [20, 21], and the current PCE of the

device based on this structure has reached 15.7% [22–25]. The compact layer has the function of blocking holes and transporting electrons and largely determines the performance of the device. An excellent compact layer requires the following characteristics: high light transmission, uniform and dense film formation, few surface defects, an energy band structure that is more compatible with perovskite materials, high electron mobility, and good hole-blocking ability. As an n-type semiconductor, SnO₂ has high electron mobility ($\sim 240 \text{ cm}^2 \text{ V}^{-1} \text{ s}^{-1}$), good UV stability, and relatively low conduction band bottom, which make it an ideal compact layer material [26–28]. There are many preparation methods of the SnO₂ layer, such as atomic layer deposition, chemical bath deposition, and spray pyrolysis [29–37]. It is also necessary to functionalize the compact layer with optimized surface contact and electrical properties for achieving superior band alignment and charge transportation in PSCs. The common optimization methods are surface treatment, metal cation doping, and composite with other materials. Rao et al. improved PCE of the device from 6.5% to 14.6% by treating

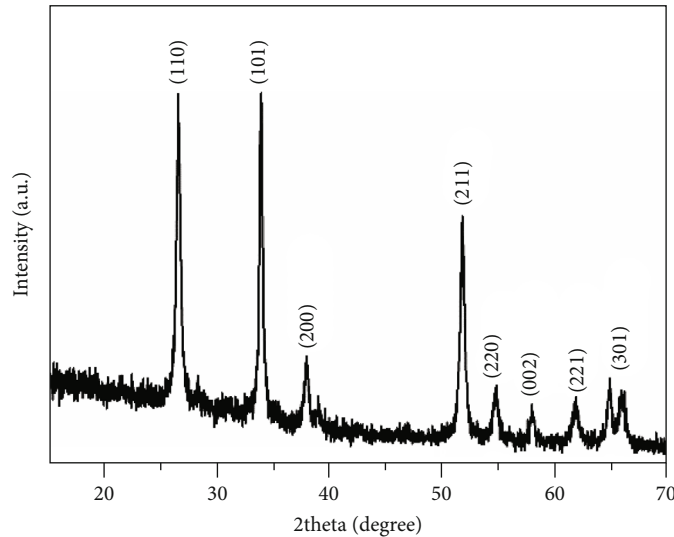


FIGURE 1: XRD diffraction pattern of Zn-SnO₂ compact layer.

the surface of the SnO₂ compact layer with aqueous TiCl₄ solution [38]. Park et al. used Li-doped SnO₂ to improve the electrical conductivity of the SnO₂ compact layer and reduce the conduction band energy of SnO₂, thereby facilitating the transfer of electrons from the perovskite layer to the compact layer, and finally achieved PCE of 18.2% [39]. Bai et al. doped the SnO₂ compact layer with Sb, which enhanced the electrical conductivity of SnO₂ and increased its Fermi energy level, allowing it to transfer more charges while effectively inhibiting the recombination of carriers, thus increasing the PCE from 15.7% to 17.2% [40]. Ren et al. prepared Nb-doped SnO₂ compact layers using a low-temperature solution-processed method to enhance the electron mobility and electrical conductivity of SnO₂, resulting in improved open-circuit voltage (V_{OC}) and fill factor (FF) of the devices and an increase of PCE from 15.3% to 17.57% [41]. Liu et al. used TiO₂ and Mg-doped SnO₂ to form a composite compact layer, which effectively utilized the advantages of the two materials to obtain a compact layer with excellent performance, and the PCE of the device was increased from 11.85% to 13.01% [42]. Successful metal cation doping can improve the coverage of the compact layer on the surface of the substrate, adjust the energy band of the compact layer to make the energy level between the compact layer and the perovskite material more match, and improve the interface contact between the compact layer and the perovskite light-absorbing layer. Besides, it can enhance the conductivity of the thin film, thus improving the performance of the device.

In this paper, we report that the Zn-doped SnO₂ compact layer can effectively enhance the electron extraction and transfer capability, which are confirmed by steady-state photoluminescence (PL) and electrochemical impedance spectroscopy (EIS) tests. The application of the Zn-doped SnO₂ compact layer in mesoporous structured PSCs with carbon electrode and without HTL has been demonstrated to effectively improve the device performance as compared to the devices with a pure SnO₂ compact layer. The Zn-doped SnO₂ compact layer-based PSCs have achieved a

PCE of 10.21%, short-circuit photocurrent current density (J_{SC}) of 19.57 mA/cm², FF of 51.58%, and V_{OC} of 1.01 V.

2. Materials and Methods

2.1. Material. Lead iodide (PbI₂, 99.99%) and TiO₂ paste (solid concentration: 20%) were purchased from Xi'an Polymer Light Technology Corp. SnCl₂·2H₂O (98%) and ZnCl₂ (98%) were purchased from Macklin. Titanium diisopropoxide bis (acetylacetonate, 75%), dimethylsulfoxide (DMSO, 99.7%), and N,N-dimethylformamide (DMF, 99.8%) were purchased from Sigma-Aldrich. Methylammonium iodide (MAI, 99.5%) and FTO (7 Ω/sq) were purchased from Yingkou Youxuan. ZrO₂ paste (solid concentration: 20%) was acquired from Shanghai MaterWin New Material. Carbon ink (10 Ω/cm²) was purchased from Jujo Printing Supplies & Technology (Pinghu) Co., Ltd. All chemicals were used without further purification.

2.2. Preparation of Zn-SnO₂ Precursor Solution. The Zn-doped SnO₂ compact layer precursor solution was prepared as follows: 0.136 g ZnCl₂ dissolved in 10 mL absolute ethanol, stirred, and fully dissolved to get 0.1 mol/L ZnCl₂ ethanol solution. The above ZnCl₂ solution was mixed with 0.1 mol/L SnCl₂·2H₂O according to the volume ratio of 0:100, 2.5:97.5, 5:95, 7.5:92.5, and 10:90; the precursor solution with 0%, 2.5%, 5%, 7.5%, and 10% mole ratio Zn doping was obtained.

2.3. Device Fabrication. Mesoporous structured PSCs were prepared by the method we reported before [43–45]. The area of the etched glass/FTO substrate is 1.5 cm × 1.5 cm, and the etched area is 0.5 cm × 1.5 cm. The etched glass/FTO substrates were pre-cleaned by immersion in acetone, isopropanol, and anhydrous ethanol in an ultrasonic box, each followed by 30 min of ultrasonication. The substrates were treated with UVO for 20 min before preparation. The Zn-doped SnO₂ compact layer precursor solution was spin-

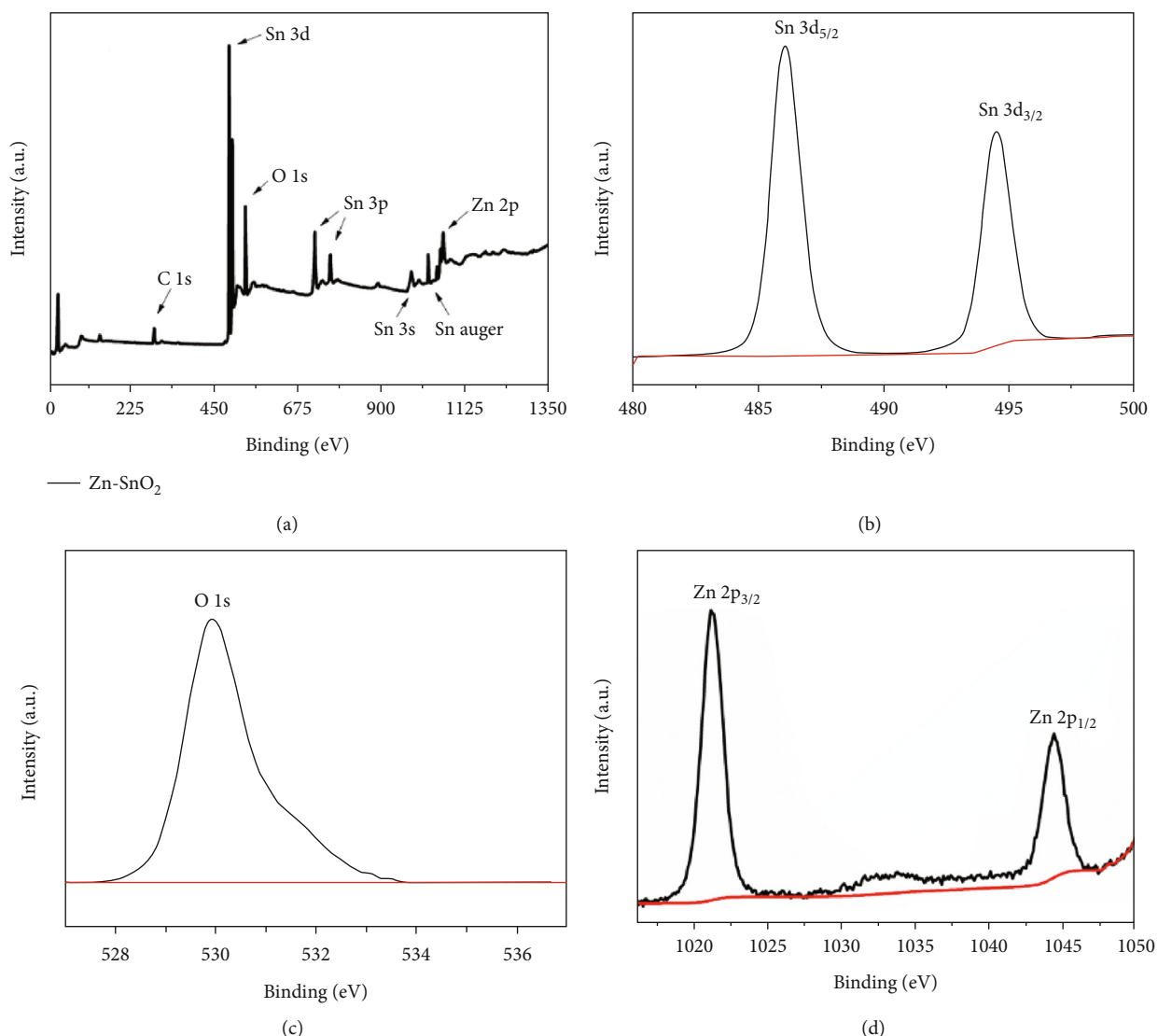


FIGURE 2: XPS spectra of (a) Zn-SnO₂ film and XPS spectra of (b) Sn 3d core level, (c) O 1s core level, and (d) Zn 2p core level peak for the Zn-SnO₂ film.

coated on the FTO glass substrate (4000 rpm, 30 s), heated at 180°C for 10 min, and sintered at 500°C for 30 min. The mesoporous TiO₂ (mp-TiO₂) layer was deposited on top of the compact film via spin-coating of the precursor of the TiO₂ mesoporous layer (mass ratio 1 : 5 TiO₂ paste to alcohol) at 3500 rpm for 20 s, followed by heating at 150°C for 10 min then sintering at 500°C for 30 min. After cooling to room temperature, the ZrO₂ layer was deposited on the device via spin-coating of the precursor of the ZrO₂ mesoporous layer (mass ratio 1 : 5 ZrO₂ paste to alcohol) at 5000 rpm for 20 s, followed by heating at 150°C for 10 min then sintering at 500°C for 30 min. The addition of ZrO₂ enhances the stability of the mesoporous structured calcium titanate solar cells [46]. The devices were transferred to the glove box and applied by one-step spin-coating using perovskite precursor solution (462 mg PbI₂ and 159 mg MAI mixed in 600 mg DMF and 78 mg DMSO) at 1000 rpm for 10 s and 4000 rpm for 30 s [46]. At the 15th second of spin-coating, 160 μL toluene was added and then heated at 100°C for 10 min. Finally,

the device was placed under the screen printing plate, and the carbon electrode with an area of 2 mm × 8 mm was scraped onto the sample and then heated at 100°C for 10 min. At this point, the whole preparation process was completed.

2.4. Characterization. The crystal structure of the devices was analyzed by an X-ray diffractometer (XRD, D8, Advance, AXS, Germany). X-ray photoelectron spectroscopy (XPS, ESCALAB 250Xi, Thermo Fisher Scientific, US) was used to analyze the element composition and chemical bonding of the devices. Cross-sectional images of the devices and morphology of nanoparticles were observed by a scanning electron microscope (SEM, JSM-IT300, JEOL, Japan). The morphology of the SnO₂ nanoparticles was analyzed by a transmission electron microscope (TEM, JEM-2100F, JEOL, Japan). Surface morphology and roughness were measured by atomic force microscopy (AFM, Nanoscope IV, VEECO, US). Steady-state photoluminescence spectroscopy (RF-6000, Shimadzu, Japan) spectra were obtained by exciting

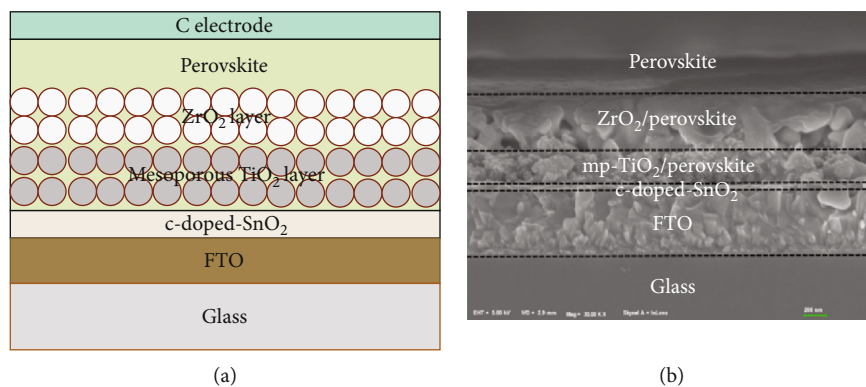


FIGURE 3: PSCs based on Zn-SnO₂ compact layer: (a) structural schematic diagram; (b) SEM cross-section.

the devices deposited on the compact layer at 500 nm. The photocurrent density-voltage (J - V) curves of the PSCs were measured by a source meter (2400, Keithley, US) and a sunlight simulator (Oriel Sol3A, Newport Corporation, US) under AM 1.5 G and light intensity of 100 mW/cm². The external quantum efficiency (EQE) of the devices was obtained by using the monochromatic incident photon-to-electron conversion efficiency spectrometer (IPCE, Newport Corporation, US). Electrochemical impedance spectroscopy measurements were performed on an electrochemical workstation (Zahner Company, Kronach, Germany) at frequencies of 0.01 MHz~4 MHz with bias voltage of 0.8 V and AM 1.5 G spectrum and light intensity of 100 mW/cm².

3. Results

The XRD spectrum of the Zn-doped SnO₂ compact layer shown in Figure 1 was obtained to investigate the crystal structure of the doped SnO₂ compact layer (c-doped-SnO₂). It shows that the SnO₂ compact layer still has good crystallinity after a small amount of Zn doping. There are strong diffraction peaks at 26.6°, 33.9°, 37.9°, 51.9°, 54.8°, 62.6°, and 65.6°, corresponding to (110, 101, 200, 211, 220, 221, and 301) of the tetragonal rutile phase SnO₂ (standard JCPDS card: 41-1445); due to the low concentration of elemental doping, no obvious diffraction peaks related to Zn²⁺ were found in the XRD pattern.

To further investigate the elemental composition and chemical bond formation in the Zn-doped SnO₂ compact layer, XPS was used to characterize the 5% Zn-SnO₂ compact layer, and the corresponding XPS spectra are shown in Figure 2. Figures 2(a) and 2(b) show the full XPS spectrum of the Zn-SnO₂ compact layer in the range of electron binding energies from 0 eV to 1350 eV, in which the characteristic peaks corresponding to Sn, O, and C elements as well as the Auger peak of Sn can be observed. Two smaller characteristic peaks appear at 1022 eV and 1045 eV, corresponding to the binding energy peak position of Zn 2p [47–49]. To observe more details of the elemental composition in the SnO₂ compact layer after doping, Figures 2(b)–2(d) show the XPS binding energy peaks of Sn 3d, O 1s, and Zn 2p. The binding energies of Sn 3d_{5/2} and Sn 3d_{3/2} appear at 485.2 eV and 493.6 eV, and the spin-orbit coupling is 8.4 eV, indicating

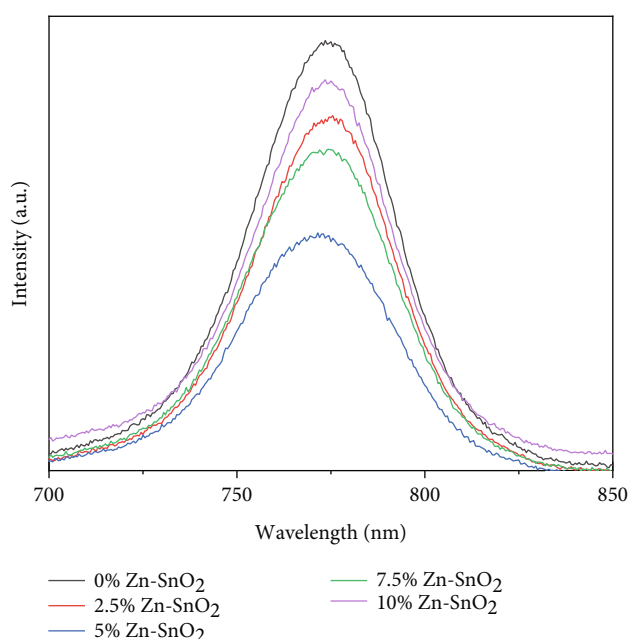


FIGURE 4: The PL spectra of PSCs with different doping concentrations of Zn-SnO₂ compact layers.

that the Sn element exists in the form of Sn⁴⁺ in the compact layer. The binding energy of O 1s appears at 530 eV, which corresponds to O²⁻. The binding energies of Zn 2p_{3/2} and Zn 2p appear at 1022 eV and 1045 eV, and the spin-orbit coupling of 22 eV corresponds to the Zn²⁺ valence state of the Zn element. The above details indicate that Zn is presented in the compact layer of SnO₂ after doping. The structural diagram and physical cross-sectional view of the Zn-SnO₂-based compact layer-based PSCs without the thick carbon counter-electrode prepared by screen printing are shown in Figure 3. The thickness of each layer in the PSC structure is FTO conductive glass ~500 nm, SnO₂ compact layer ~40 nm, the mixed layer of mesoporous TiO₂ and CH₃NH₃PbI₃ ~150 nm, the mixed layer of mesoporous ZrO₂ and CH₃NH₃PbI₃ ~150 nm, and CH₃NH₃PbI₃ cap layer over the mixed layers ~300 nm.

The PL spectrum was used to characterize the photoluminescence of CH₃NH₃PbI₃ grown on a glass substrate with

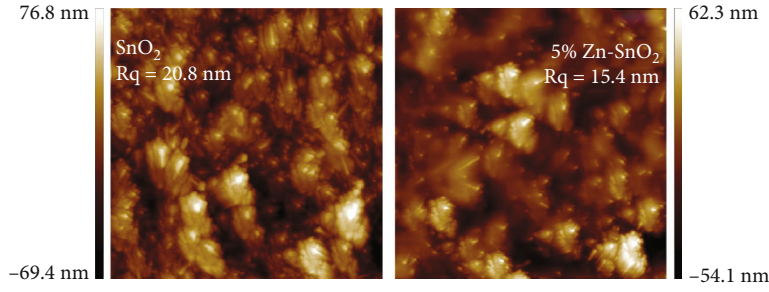


FIGURE 5: AFM topographic images (top) for c-SnO₂ films with and without Zn doping.

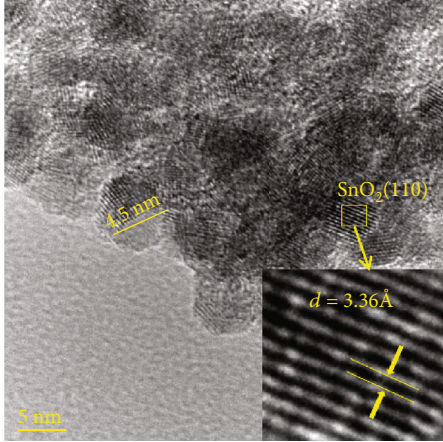


FIGURE 6: TEM image of 5% Zn-SnO₂ nanoparticles.

Zn-SnO₂ compact layers deposited from different doping concentrations of precursors under an excitation wavelength of 500 nm. As seen from Figure 4, the peak of the PL spectra occurs at 775 nm, when the fluorescence intensity is strongest. The lower peak intensity of the PL spectra means that the photoinduced charge carriers from CH₃NH₃PbI₃ were extracted and quickly transferred to the compact layer, resulting in a quenching effect that reduces the peak intensity. As the doping amount of Zn in the compact layer continues to increase, the emission peak intensity rises again, and the lowest emission of the perovskite layer is obtained on the SnO₂ compact layer with 5% Zn doping, indicating the highest electron extraction rate. Figure 5 shows the surface morphology of undoped and Zn-doped SnO₂ compact layers. Root-mean-squared roughness (Rq) decreases after the doping of Zn; the Rq of the undoped SnO₂ film is 20.8 nm; after Zn doping, it decreased to 15.4 nm. Combined with Figure 4, it is shown that Zn-doped SnO₂ provides a smoother surface and better electrical properties, which is the best ETL for the perovskite layer. Figure 6 shows nanoparticles of the compact layer. It shows that the dispersion of SnO₂ nanoparticles in ethylene glycol is not good and there are agglomerations. At the edge, it can be seen that the size of the nanoparticles is very uniform and the particle size is about 4.5 nm. As shown in Figure 6, SnO₂ nanoparticles with a lattice spacing of 3.36 Å correspond to the crystal planes of the SnO₂ crystal (110).

Under the irradiation of simulated standard sunlight (AM 1.5 G, 100 mW/cm²), the photovoltaic characteristics

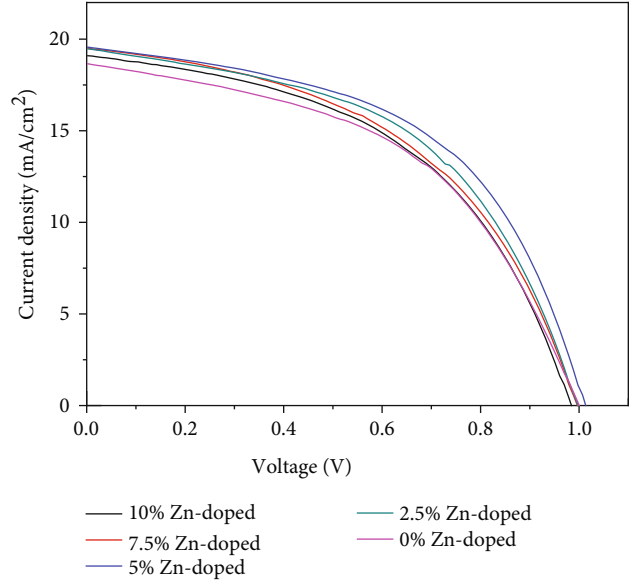


FIGURE 7: J - V curves of PSCs based on Zn-SnO₂ compact layers with different doping concentrations.

TABLE 1: Photoelectric parameters of PSCs based on Zn-SnO₂ compact layers with different doping concentrations.

Compact layer	J_{SC} (mA/cm ²)	V_{OC} (V)	FF (%)	PCE (%)
SnO ₂	19.11	0.98	48.36	9.08
2.5% Zn-SnO ₂	19.51	0.99	49.65	9.64
5% Zn-SnO ₂	19.57	1.01	51.58	10.21
7.5% Zn-SnO ₂	19.47	1	50.1	9.77
10% Zn-SnO ₂	19.25	1	47.58	9.19

of PSCs were tested and characterized with a digital source meter at a rate of 0.15 V/s in the room ambient condition. The J - V curves of PSCs based on different doping levels of Zn-SnO₂ compact layers are shown in Figure 7, and the photovoltaic parameters are shown in Table 1. Figure 8 is the corresponding distribution of PCE distribution. According to Figure 7 and Table 1, we can conclude that J_{SC} , FF, and PCE of Zn-SnO₂ compact layer-based PSCs increase with the increase of Zn²⁺ doping concentration and reach the largest value at 5% Zn²⁺ doping concentration. After the Zn²⁺ doping SnO₂ compact layer, J_{SC} of PSCs based on the Zn-SnO₂ compact layer increased from 19.11 mA/cm² to 19.57

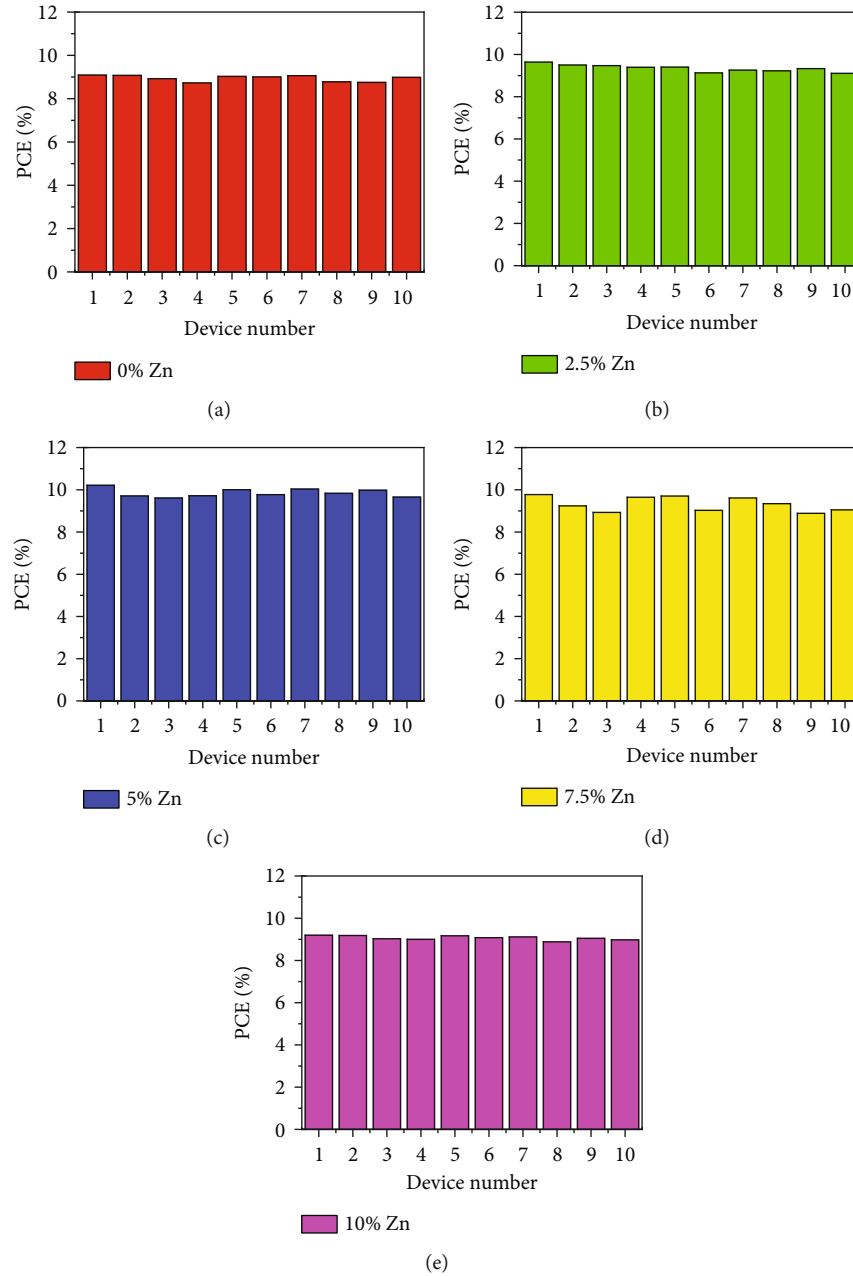


FIGURE 8: PCE distribution of PSCs based on Zn-SnO₂ compact layers with different doping concentrations.

mA/cm², the FF increased from 48.36% to 51.58%, and the PCE increased from 9.08% to 10.21%. As the Zn²⁺ doping concentration continued to increase, the performance of the PSCs based on the Zn-SnO₂ compact layer decreases. The reason is that excessive doping will affect the crystallization of SnO₂ and provide nonradiative carrier recombination centers, resulting in the decrease of J_{SC} , FF, and PCE. It is noticed that V_{OC} was almost unchanged. V_{OC} is related to the energy level matching among each layer, thus indicating that the moderate amount of doping does not have a large impact on the SnO₂ energy band. The performance of PSCs is optimal when the Zn²⁺ doping concentration is 5%, and the device performance is improved by 12.4% compared to the PSCs based on the SnO₂ compact layer without doping.

The IPCE of the pure SnO₂ compact layer and 5% Zn-SnO₂ compact layer PSCs were measured and characterized using a quantum efficiency measurement system. The IPCE curves and matching integral current curves are shown in Figure 9. It is observed that the IPCE curves of the two PSCs show a similar trend, and the IPCE value in the visible range of the 5% Zn-SnO₂ compact layer-based device was higher than that of the pure SnO₂ compact layer-based device, indicating that the carrier extraction and transfer capability is enhanced by the doping of Zn²⁺. Besides, the integration of the IPCE curve from the 5% Zn-SnO₂ compact layer and pure SnO₂ compact layer devices is obtained to be 19.46 mA/cm² and 19.08 mA/cm², which are consistent with the J_{SC} values measured in the $J-V$ curves.

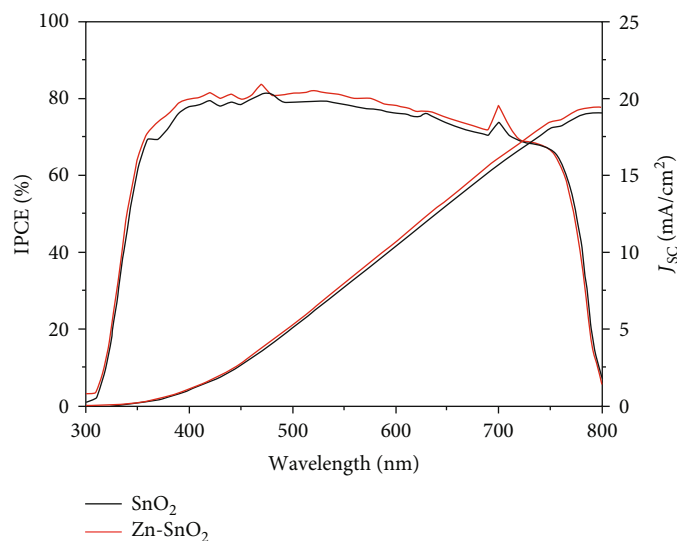


FIGURE 9: IPCE and current integral curves based on pure SnO_2 compact layer and 5% Zn-SnO_2 compact layer PSCs.

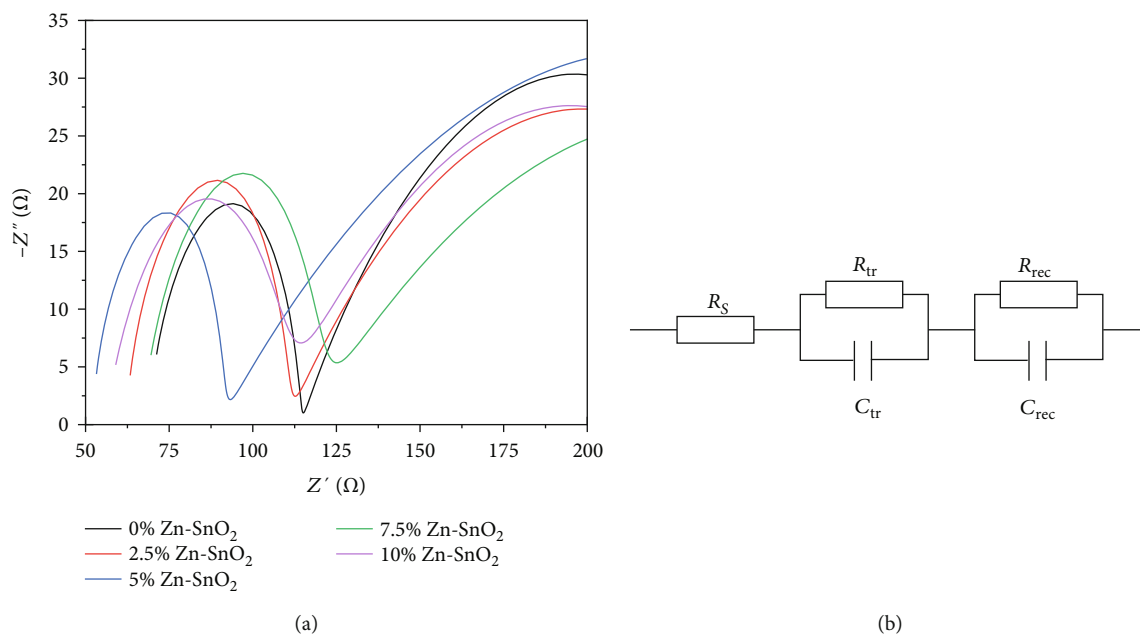


FIGURE 10: (a) Nyquist diagram of PSCs based on different doping concentrations of Zn-SnO_2 compact layer; (b) equivalent circuit to fit the Nyquist curve.

The EIS of PSCs based on different concentrations of Zn^{2+} -doped SnO_2 compact layer and pure SnO_2 compact layer were tested and characterized to further investigate the carrier transport characteristics. The EIS spectrum and equivalent circuit diagram are shown in Figure 10. There are two semicircles in the Nyquist diagram. The left semicircle corresponds to the high-frequency region, which reflects the interface contact between the perovskite light-absorbing layer and the carbon electrode and is shown in the form of transfer resistance (R_{tr}) in the equivalent circuit. The right semicircle corresponds to the low-frequency region, reflecting the interface contact between the perovskite light-

absorbing layer and the ETL, and is expressed in the form of composite resistance (R_{rec}) in the equivalent circuit [50]. The values of the individual resistances in the equivalent circuit fitted from the Nyquist plot are shown in Table 2. From the data in the table, it can be concluded that the R_{rec} value of the device based on the 5% Zn^{2+} -doped SnO_2 compact layer is the largest, which indicates that the Zn-SnO_2 compact layer has a good ability of electron extraction and transfer and can quickly transfer the electrons generated by perovskite materials to the substrate electrode. The contact resistance of R_s value in 5% Zn^{2+} -doped SnO_2 compact layer device is the smallest, which means that the device has higher FF.

TABLE 2: EIS parameters of Zn-SnO₂ compact layer PSCs with different Zn²⁺ doping concentrations.

Zn ²⁺ doping ratio (%)	R_s (Ω)	R_{tr} (Ω)	R_{rec} (Ω)
0	69	45.5	159
2.5	62.1	48.2	173
5	52	38.3	250.7
7.5	66.3	50.6	222
10	56.1	52	169.8

Generally speaking, the contact resistance R_s value of the pure SnO₂ compact layer is the largest, which is also consistent with the conclusion drawn from the J - V curves. Because the upper surface of perovskite materials of the two devices is deposited with carbon electrode, a strict preparation process will not lead to a great difference in carbon electrode; the transfer resistance R_{tr} values are close.

4. Conclusions

In the study, Zn²⁺ (~74 pm), which has a similar ionic radius to Sn⁴⁺ (~72 pm), was introduced to dope into the SnO₂ compact layer. By controlling the proportion of Zn²⁺ in the SnCl₂·2H₂O precursor solution, Zn-SnO₂ compact layers with different doping concentrations were prepared and applied to PSCs. XRD, XPS, SEM, EIS, and PL were used to characterize and analyze the surface morphology, crystal structure and crystallinity, element composition, and chemical bond formation of the SnO₂ compact layer. PL and EIS spectra of PSCs based on the Zn-SnO₂ compact layer with different doping concentrations were tested and analyzed to explain the change of electron extraction ability of the compact layer after doping. The peak intensity of the PL spectrum decreased after Zn²⁺ doping and reached the lowest when the doping concentration was 5%. According to the fitting data from the Nyquist diagram measured by EIS, the composite resistance R_{rec} value of devices based on the Zn-SnO₂ compact layer is higher than that of devices based on the pure SnO₂ compact layer, indicating that it has good conductivity and can effectively transfer electrons, thereby reducing the carrier recombination. The J - V curves of PSCs based on the SnO₂ compact layer with different Zn²⁺ doping concentrations were tested and characterized. Compared with the devices without the doping SnO₂ compact layer, when the Zn²⁺ doping concentration was 5%, the performance of the Zn-SnO₂ compact layer device was the best. The PCE increased from 9.08% to 10.21%, with an increase of 12.4%.

Data Availability

The XRD, XPS, SEM, PL, AFM, J - V , IPCE, and EIS data used to support the findings of this study are included within the article.

Conflicts of Interest

The authors declare no conflict of interest.

Authors' Contributions

Conceptualization was handled by M.C. and C.Y.; experiment was taken care of by C.Y., M.C., and J.W.; data curation was managed by C.Y., J.W., and H.L.; writing (original draft) was performed by C.Y. and M.C.; and writing (review and editing) was made by C.Y., M.C., J. W., and H.L.

Acknowledgments

This research was funded by the National innovation and entrepreneurship training program for college students (202010497048) and the Natural Science Foundation of China (NSFC) (11704293 and 11974266).

References

- [1] Y. C. Shao, Y. B. Yuan, and J. S. Huang, "Correlation of energy disorder and open-circuit voltage in hybrid perovskite solar cells," *Nature Energy*, vol. 1, no. 1, 2016.
- [2] X. P. Zheng, B. Chen, J. Dai et al., "Defect passivation in hybrid perovskite solar cells using quaternary ammonium halide anions and cations," *Nature Energy*, vol. 2, no. 7, 2017.
- [3] J. H. Noh, S. H. Im, J. H. Heo, T. N. Mandal, and S. I. Seok, "Chemical management for colorful, efficient, and stable inorganic-organic hybrid nanostructured solar cells," *Nano Letters*, vol. 13, no. 4, pp. 1764–1769, 2013.
- [4] S. D. Stranks, G. E. Eperon, G. Grancini et al., "Electron-hole diffusion lengths exceeding 1 micrometer in an organometal trihalide perovskite absorber," *Science*, vol. 342, no. 6156, pp. 341–344, 2013.
- [5] A. Kojima, K. Teshima, Y. Shirai, and T. Miyasaka, "Organometal halide perovskites as visible-light sensitizers for photovoltaic cells," *Journal of the American Chemical Society*, vol. 131, no. 17, pp. 6050–6051, 2009.
- [6] H. S. Kim, C. R. Lee, J. H. Im et al., "Lead iodide perovskite sensitized all-solid-state submicron thin film mesoscopic solar cell with efficiency exceeding 9%," *Scientific Reports*, vol. 2, no. 1, 2012.
- [7] L. Etgar, P. Gao, Z. S. Xue et al., "Mesoscopic CH₃NH₃PbI₃/TiO₂ heterojunction solar cells," *Journal of the American Chemical Society*, vol. 134, no. 42, pp. 17396–17399, 2012.
- [8] A. Y. Mei, X. Li, L. F. Liu et al., "A hole-conductor-free, fully printable mesoscopic perovskite solar cell with high stability," *Science*, vol. 345, no. 6194, pp. 295–298, 2014.
- [9] National Renewable Energy Laboratory (NREL), *Best research-cell efficiencies chart*, 2020, <https://www.nrel.gov/pv/assets/pdfs/best.research-cell-efficiencies.20200218.pdf>.
- [10] P. Y. Gu, N. Wang, A. Y. Wu et al., "An azaacene derivative as promising electron-transport layer for inverted perovskite solar cells," *Chemistry, an Asian Journal*, vol. 11, no. 15, pp. 2135–2138, 2016.
- [11] A. A. Said, J. Xie, and Q. C. Zhang, "Recent progress in organic electron transport materials in inverted perovskite solar cells," *Small*, vol. 15, no. 27, p. 1900854, 2019.
- [12] A. A. Said, J. Xie, Y. Wang et al., "Efficient inverted perovskite solar cells by employing N-type (D–A1–D–A2) polymers as electron transporting Layer," *Small*, vol. 15, no. 29, 2019.
- [13] S. Yakunin, L. Protesescu, F. Krieg et al., "Low-threshold amplified spontaneous emission and lasing from colloidal

- nanocrystals of caesium lead halide perovskites,” *Nature Communications*, vol. 6, no. 1, 2015.
- [14] G. C. Xing, N. Mathews, S. Y. Sun et al., “Long-range balanced electron- and hole-transport lengths in organic-inorganic $\text{CH}_3\text{NH}_3\text{PbI}_3$,” *Science*, vol. 342, no. 6156, pp. 344–347, 2013.
- [15] G. C. Xing, B. Wu, X. Y. Wu et al., “Transcending the slow bimolecular recombination in lead-halide perovskites for electroluminescence,” *Nature Communications*, vol. 8, no. 1, 2017.
- [16] G. C. Xing, M. H. Kumar, W. K. Chong et al., “Solution-processed tin-based perovskite for near-infrared lasing,” *Advanced Materials*, vol. 28, no. 37, pp. 8191–8196, 2016.
- [17] G. E. Eperon, S. D. Stranks, C. Menelaou, M. B. Johnston, L. M. Herz, and H. J. Snaith, “Formamidinium lead trihalide: a broadly tunable perovskite for efficient planar heterojunction solar cells,” *Energy & Environmental Science*, vol. 7, no. 3, pp. 982–988, 2014.
- [18] J. Burschka, N. Pellet, S. J. Moon et al., “Sequential deposition as a route to high-performance perovskite-sensitized solar cells,” *Nature*, vol. 499, no. 7458, pp. 316–319, 2013.
- [19] Q. Chen, H. P. Zhou, Z. R. Hong et al., “Planar heterojunction perovskite solar cells via vapor-assisted solution process,” *Journal of the American Chemical Society*, vol. 136, no. 2, pp. 622–625, 2014.
- [20] L. W. Abu and L. Etgar, “Depleted hole conductor-free lead halide iodide heterojunction solar cells,” *Energy & Environmental Science*, vol. 6, no. 11, pp. 3249–3253, 2013.
- [21] A. Yella, L. P. Heiniger, P. Gao, M. K. Nazeeruddin, and M. Gratzel, “Nanocrystalline rutile electron extraction layer enables low-temperature solution processed perovskite photovoltaics with 13.7% efficiency,” *Nano letters*, vol. 14, no. 5, pp. 2591–2596, 2014.
- [22] Y. Hu, Z. H. Zhang, A. Y. Mei et al., “Improved performance of printable perovskite solar cells with bifunctional conjugated organic molecule,” *Advanced Materials*, vol. 30, no. 11, 2018.
- [23] H. N. Chen and S. H. Yang, “Carbon-based perovskite solar cells without hole transport materials: the front runner to the market?,” *Advanced Materials*, vol. 29, no. 24, 2017.
- [24] L. Xu, Y. Xiong, A. Y. Mei et al., “Efficient perovskite photovoltaic-thermoelectric hybrid device,” *Advanced Energy Materials*, vol. 8, no. 13, 2018.
- [25] M. Acik, Darling, and B. Seth, “Graphene in perovskite solar cells: device design, characterization and implementation,” *Journal of Materials Chemistry A*, vol. 4, no. 17, pp. 6185–6235, 2016.
- [26] J. B. You, L. Meng, T. B. Song et al., “Improved air stability of perovskite solar cells via solution-processed metal oxide transport layers,” *Nature Nanotechnology*, vol. 11, no. 1, pp. 75–81, 2016.
- [27] W. Ke, G. Fang, Q. Liu et al., “Low-temperature solution-processed tin oxide as an alternative electron transporting layer for efficient perovskite solar cells,” *Journal of the American Chemical Society*, vol. 137, no. 21, pp. 6730–6733, 2015.
- [28] X. K. Huang, Z. Y. Hu, J. Xu et al., “Low-temperature processed SnO_2 compact layer by incorporating TiO_2 layer toward efficient planar heterojunction perovskite solar cells,” *Solar Energy Materials & Solar Cells*, vol. 164, pp. 87–92, 2017.
- [29] G. Yang, P. L. Qin, G. J. Fang, and G. Li, “Tin oxide (SnO_2) as effective electron selective layer material in hybrid organic-inorganic metal halide perovskite solar cells,” *Journal of Energy Chemistry*, vol. 27, no. 4, pp. 962–970, 2018.
- [30] G. Yang, C. Chen, F. Yao et al., “Effective carrier-concentration tuning of SnO_2 quantum dot electron-selective layers for high-performance planar perovskite solar cells,” *Advanced Materials*, vol. 30, no. 14, p. 1706023, 2018.
- [31] L. Kavan, L. Steier, and M. Gratzel, “Ultrathin buffer layers of SnO_2 by atomic layer deposition: perfect blocking function and thermal stability,” *Journal of Physical Chemistry C*, vol. 121, no. 1, pp. 342–350, 2017.
- [32] J. P. C. Baena, L. Steier, W. Tress et al., “Highly efficient planar perovskite solar cells through band alignment engineering,” *Energy & Environmental Science*, vol. 8, no. 10, pp. 2928–2934, 2015.
- [33] D. P. McMeekin, G. Sadoughi, W. Rehman et al., “A mixed-cation lead mixed-halide perovskite absorber for tandem solar cells,” *Science*, vol. 351, no. 6269, pp. 151–155, 2016.
- [34] J. Barbe, M. L. Tietze, M. Neophytou et al., “Amorphous tin oxide as a low-temperature-processed electron-transport layer for organic and hybrid perovskite solar cells,” *ACS Applied Materials & Interfaces*, vol. 9, no. 13, pp. 11828–11836, 2017.
- [35] Y. Li, J. Zhu, Y. Huang et al., “Mesoporous SnO_2 nanoparticle films as electron-transporting material in perovskite solar cells,” *RSC Advances*, vol. 5, no. 36, pp. 28424–28429, 2015.
- [36] X. X. Jiang, Y. L. Xiong, Z. H. Zhang et al., “Efficient hole-conductor-free printable mesoscopic perovskite solar cells based on SnO_2 compact layer,” *Electrochimica Acta*, vol. 263, pp. 134–139, 2018.
- [37] M. Singh, A. Ng, Z. W. Ren et al., “Facile synthesis of composite tin oxide nanostructures for high-performance planar perovskite solar cells,” *Nano Energy*, vol. 60, pp. 275–284, 2019.
- [38] H. S. Rao, B. X. Chen, W. G. Li et al., “Improving the extraction of photogenerated electrons with SnO_2 nanocolloids for efficient planar perovskite solar cells,” *Advanced Functional Materials*, vol. 25, no. 46, pp. 7200–7207, 2015.
- [39] M. Park, J. Y. Kim, H. J. Son, C. H. Lee, S. S. Jang, and M. J. Ko, “Low-temperature solution-processed Li-doped SnO_2 as an effective electron transporting layer for high-performance flexible and wearable perovskite solar cells,” *Nano Energy*, vol. 26, pp. 208–215, 2016.
- [40] Y. Bai, Y. J. Fang, Y. H. Deng et al., “Low temperature solution-processed Sb: SnO_2 nanocrystals for efficient planar perovskite solar cells,” *Chem*, vol. 9, no. 18, pp. 2686–2691, 2016.
- [41] X. D. Ren, D. Yang, Z. Yang et al., “Solution-processed Nb: SnO_2 electron transport layer for efficient planar perovskite solar cells,” *ACS Applied Materials & Interfaces*, vol. 9, no. 3, pp. 2421–2429, 2017.
- [42] N. Liu, M. W. Chen, H. Yang et al., “ $\text{TiO}_2/\text{Mg}-\text{SnO}_2$ nanoparticle composite compact layer for enhancing the performance of perovskite solar cells,” *Optical Materials Express*, vol. 10, no. 1, pp. 157–169, 2020.
- [43] B. Wang, X. Y. Zhu, S. H. Li, M. W. Chen, H. F. Lu, and Y. P. Yang, “Ag@ SiO_2 core-shell nanoparticles embedded in a TiO_2 mesoporous layer substantially improve the performance of perovskite solar cells,” *Nanomaterials*, vol. 8, no. 9, p. 701, 2018.
- [44] J. H. Hu, W. H. Liu, Y. P. Yang et al., “ TiO_2 nanotube/ TiO_2 nanoparticle hybrid photoanode for hole-conductor-free perovskite solar cells based on carbon counter electrodes,” *Optical Materials Express*, vol. 7, no. 9, pp. 3322–3331, 2017.
- [45] S. H. Li, X. Y. Zhu, B. Wang et al., “Influence of Ag nanoparticles with different sizes and concentrations embedded in a

- TiO₂ compact layer on the conversion efficiency of perovskite solar cells,” *Nanoscale Research Letters*, vol. 13, no. 1, p. 210, 2018.
- [46] Y. G. Rong, Z. L. Ku, A. Y. Mei et al., “Hole-conductor-free mesoscopic TiO₂/CH₃NH₃PbI₃ heterojunction solar cells based on anatase nanosheets and carbon counter electrodes,” *Journal of Physical Chemistry Letters*, vol. 5, no. 12, pp. 2160–2164, 2014.
- [47] B. Thomas and B. Skariah, “Spray deposited Mg-doped SnO₂ thin film LPG sensor: XPS and EDX analysis in relation to deposition temperature and doping,” *Journal of Alloys and Compounds*, vol. 625, pp. 231–240, 2015.
- [48] X. C. Dou, D. Sabba, N. Mathews, L. H. Wong, Y. M. Lam, and S. Mhaisalkar, “Hydrothermal synthesis of high electron mobility Zn-doped SnO₂ Nanoflowers as photoanode material for efficient dye-sensitized solar cells,” *Chemistry of Materials*, vol. 23, no. 17, pp. 3938–3945, 2011.
- [49] E. Ramasamy and J. Lee, “Ordered mesoporous Zn-doped SnO₂ synthesized by exotemplating for efficient dye-sensitized solar cells,” *Energy & Environmental Science*, vol. 4, no. 7, pp. 2529–2536, 2011.
- [50] E. Ghahremanirad, A. Bou, S. Olyaei, and J. Bisquert, “Inductive loop in the impedance response of perovskite solar cells explained by surface polarization model,” *Journal of Physical Chemistry Letters*, vol. 8, no. 7, pp. 1402–1406, 2017.